

Synthesis and Characterization of ZnS Nanosized Semiconductor Particles within Mesoporous Solids

K. Dimos,[†] I. B. Koutselas,[‡] and M. A. Karakassides^{*,†}

Department of Materials Science and Engineering, University of Ioannina, Ioannina 45110, Greece, and
Department of Materials Science, University of Patras, Patras 26504, Greece

Received: July 7, 2006; In Final Form: August 31, 2006

ZnS semiconductor quantum dots have been synthesized using a method involving melt exchange reaction inside the pores of MCM-41 and subsequent reaction with H₂S. The ZnS quantum dots–MCM-41 composite, which has been studied with XRD, EDS, and BET techniques, is shown to have retained within the pores the formed quantum dots, with a size distribution exhibiting a maximum nanoparticle diameter of ca. 1.8 nm. The structure and the sorption properties of the ZnS/MCM-41 composite have been studied by means of X-ray diffraction, Fourier transform infrared spectroscopy, and surface area measurements. All experimental data reveal that all the final composite products, containing up to 9.3 wt % ZnS as verified by EDS analysis, keep the basic structural characteristics of MCM-41 materials, without significant reduction of their active surface areas. The quantum dot optical properties have been studied with UV–vis, photoluminescence, and photoluminescence excitation spectroscopies providing evidence for the low-dimensional character of the ZnS semiconductor particles.

1. Introduction

Semiconducting solids have been an active research subject during the past 50 years. Lately, it has been found that in addition to the naturally occurring three-dimensional (3D) semiconductor systems it is possible to synthesize artificially (e.g., with molecular beam epitaxy) or naturally (e.g., with solid-state chemistry) low-dimensional (LD) semiconductor systems, such as the two-dimensional (2D), one-dimensional (1D), and zero-dimensional (0D) systems.¹ These in many cases are known as quantum wells, quantum wires, and quantum dots, respectively. These three latter possess outstanding physical, physicochemical, and/or chemical properties. Also, due to their present and future applicability in electronic devices, light-emitting diodes, sensors, and nonlinear optical devices, a lot of effort goes into creating structurally well-defined nanostructures. In this approach, it is possible to tune the properties of the LD systems by tailoring the structure of the material in the atomic scale and nanoscale. LD systems are promising because most of the electrical and optical phenomena are strong manifestations of the quantum description of electrons within confined spaces. The size quantization effects become very interesting, as far as the semiconductor energy gap (E_g) and the excitonic states that lie within the energy gap, when the system size becomes smaller than the electron's thermal de Broglie wavelength. These effects were first observed in CdS particles.^{2–4}

In past years various materials that provide distinct defined cavities have been used to synthesize nanostructured semiconductors. For example, zeolites,^{5–7} micelles,^{8–11} polymers,^{12,13} and molecular sieves^{14–17} have been used to restrict growth. Among these, using highly ordered mesoporous solids as hosts for limiting the growth of semiconductors inside their pores is

a very promising scheme for preparation, thus achieving controlled dimension and morphology. The MCM-41 solid, a member of the M41S family, exhibits regular hexagonal arrays of cylinder-like pores and a variable pore diameter between 1.5 and 20 nm.^{18,19} Its large surface area makes it ideal for catalytic applications as well as the loading of it with metal cations. Its preparation with organic precursors also makes it ideal to create mesoporous solids where the cylinders are not only filled with nanosized semiconductor materials but also with organic molecules that can be used for energy exchange between the quantum dots and the organic molecules, also called Forster type energy transfer—a phenomenon that is accompanied by a variety of physical and chemical phenomena.²⁰

ZnS has a large direct band gap energy of 3.68 or 3.91 eV in the cubic or hexagonal form, respectively. The Bohr excitonic radius in the 3D ZnS system is about 22 Å with a binding energy of about 36 meV, which makes it undetectable in room temperature (RT) measurements. When it is in the form of a quantum dot, the band gap shifts toward higher energies, also named “blue shift”. Both the 3D system and the ZnS quantum dot have allowed direct optical transition at the Γ point, and thus all band gap and excitonic effects can be observed. The excitonic pair, electron–hole, is usually spread on the surface of the quantum dot (QD) when the size is around 20 Å. These last arguments position the ZnS QD systems as interesting systems to study in order to understand the tuning capabilities of its absorbance and luminescence peaks in relation to their synthesis and their host environment, for future devices.

The preparation of ZnS nanoparticles inside ordered mesoporous silica has received considerable attention because the morphology of these materials provides not only the template to grow and contain the individuality of the ZnS quantum dots but also a way to keep the quantum dot size. By disallowing the quantum dot interaction, the optical effects become sharper and simpler to analyze. In the case of the MCM-41 only the ZnS quantum dots that could interact are the ones that have

* Corresponding author. Telephone: +3026510 97276. Fax: +3026510 97074. E-mail address: mkarakas@cc.uoi.gr.

[†] University of Ioannina.

[‡] University of Patras.

been grown within the same pore. However, in the results and discussion section it will become obvious that in the presented synthesis the ZnS quantum dots are practically isolated.

In this research work, a new method is reported, added to the few existing similar works,^{16,21,22} where the MCM-41 remains intact after the insertion of Zn^{2+} and later of ZnS nanoparticles, without the formation of the latter outside the pores. Other methods have also been followed, for comparison, which clearly force the creation of ZnS nanoparticles outside the pores. The method is based on melt exchange reactions between the positively charged template molecules in an as-synthesized MCM-41 material of the S^+I^- type (S^+ stands for ionic surfactant and I^- for the silica network) and positively charged metal-containing oligonuclear clusters derived from low melting point zinc(II) nitrate salt. The method proceeds in the solid state and enables a uniform loading of the silica surfaces with a high amount of metal without destroying the organized architecture of the parent MCM-41 material.²³ The final ZnS nanocrystals were formed after reaction of the Zn^{2+} -MCM-41 sample with H_2S gas. The porosity of the final structure remains high, thus making the nanosemiconductor-MCM composite usable for catalytic and photocatalytic applications, via the enhanced properties of the ZnS excitonic surface states. The main advantages of the reported method is the possibility to incorporate high concentrations of metal centers in the silica framework and their homogeneous distribution in the resulting porous structure, preserving, however, the high porosity of the matrix. The later makes efficient the study of fluorescence properties and the evaluation and comparison of ZnS nanoparticles confined in these siliceous MCM-41 channels with that embedded in porous sol-gel or ordered mesoporous silicas in previous works. The preparation stages, the structures, and the sorption properties of the obtained materials were studied by means of X-ray diffraction (XRD), Fourier transform infrared spectroscopy (FT-IR), and surface area measurements. The nature and the optical properties of nanosemiconductors were examined using UV-vis and photoluminescence spectroscopies.

2. Experimental Section

2.1 Preparation. The MCM-41 sample was synthesized by hydrolyzing 10.5 g of cetyltrimethylammonium bromide (CTABr) and 50 g of tetraethyl orthosilicate (TEOS), each one being in this order added in an 1 L polyethylene bottle containing 417.5 g of H_2O and 268.5 g of NH_3 (25 wt %). Each of the previous additions was stirred for 30 min. The product was retrieved after heat treatment at 80 °C for 96 h, which can be slightly considered as a hydrothermal treatment. It was filtered, rinsed with cold ethanol (EtOH), and finally placed on a plate for air-drying (hereafter named AS-MCM-41). A part of the MCM-41 batch was heat treated at 600 °C in order to use it as reference material in surface area measurements (HT-MCM-41).

The salt $\text{Zn}(\text{NO}_3)_2 \cdot 6\text{H}_2\text{O}$ (mp 36 °C) was employed for the melt exchange reactions. In a typical preparation, 0.5 g of MCM-41 solid was well ground with a large excess of the corresponding salt (1 g) and the solid mixture was heated at 80 °C for 3.5 h. Then, each mixture was cooled to room temperature and subsequently washed very well with hot ethanol prior to drying. The product was filtered and rinsed with cold EtOH. The same procedure was repeated for the final product to increase the yield of Zn^{2+} loading. Finally, the end product was placed on a plate for air-drying (Zn-MCM-41). The ZnS-loaded MCM-41 sample has been prepared by dissolving 100 mg of the Zn^{2+} -loaded MCM-41 sample in 50 mL of EtOH. The solution was then treated with H_2S . Various samples have been obtained for

various times and flow rates of H_2S treatment. The best samples were obtained for 30 min at a flow of about 3 mL/s (ZnS-MCM-41). Moreover, a part of the ZnS-MCM-41 sample was heated at 600 °C in order to check the capability of the composite to retain its mesoporous structure (ZnSHT-MCM-41) after treatment at high temperatures.

Samples of quantum dot composites have also been prepared with small sulfur content, i.e., with small flow rate and exposure time reaction, for reference in optical experiments (ZnS₀-MCM-41). Also, reference samples for ZnS bulklike nanoparticles were synthesized by precipitation of the nanocrystals when H_2S was passed through a solution of $\text{Zn}(\text{NO}_3)_2 \cdot 6\text{H}_2\text{O}$ in ethanol and were also characterized. The final sample was retrieved by filtration with a Gooch crucible and rinsed with EtOH.

2.2 Characterization. X-ray powder diffraction data were collected on a D8 Advance Bruker diffractometer using Cu K α (40 kV, 40 mA, $\lambda = 1.54178 \text{ \AA}$) radiation and a secondary beam graphite monochromator. Diffraction patterns were collected in the 2θ range from 2 to 80°, in steps of 0.02° and 2 s counting time per step. Energy-dispersive spectra were collected using a JEOL JSM-5600 scanning electron microscope (SEM) using a sample holder of the composition 39% Zn-61% Cu. The Cu composition specified the Zn sample percentage, which was automatically subtracted from the measured data. The analysis results were the average of five different region surface measurements of each sample.

Infrared spectra were measured on a Perkin-Elmer GX, Fourier transform spectrometer in the frequency range of 400–2000 cm^{-1} . Samples were dispersed pulverized in the form of KBr pellets used for recording the spectra, which were the average of 32 scans at 2 cm^{-1} resolution.

The N_2 adsorption-desorption isotherms were measured at 77 K on a Sorptomatic 1990, thermo Finnigan porosimeter. Specific surface areas S_{BET} were determined with the Brunauer-Emmett-Teller (BET) method using adsorption data points in the relative pressure P/P_0 range 0.01–0.30. Surface areas S_i were also determined from t -plots, which were constructed using nitrogen adsorption data on a nonporous hydroxylated silica standard. The desorption branches of the isotherms were used for the pore size calculations according to the Kelvin equation $r_k \sim 4.146/(\log P_0/P) \text{ (\AA)}$, where P_0 is the saturated vapor pressure in equilibrium with the adsorbate condensed in a capillary or a pore, P is the vapor pressure of a liquid contained in a cylindrical capillary, and r_k is the Kelvin radius of the capillary or pore. The Kelvin equation was used according to the Barrett-Joyner-Halenda (BJH) method for calculation of core radii from the pressure values of the isotherm, the pore radius combining the last with the t -values from the standard isotherm, and finally the pore size distribution (PSD) of the samples. All samples used for the surface analyses were outgassed at 250 °C for 10 h under high vacuum (10^{-5} mbar) before the measurements.

UV-vis spectra were recorded on a Shimadzu UV-2401PC two-beam spectrophotometer in the range of 200–800 nm, at a step of 0.5 nm, using a combination of deuterium and halogen lamps as sources. The presented spectra were obtained from thin film transmission measurements by rubbing the samples on quartz. These have also been confirmed to be the same as those obtained from diffuse reflectance experiments of solid pressed pellets, through the Kubelka-Monk relation.

The photoluminescence (PL) spectra were obtained from solid pressed pellets mounted in a Jobin Yvon Fluorolog 3 spectrofluorometer FL-11 employing a xenon 450 W lamp and a P928P photodetector. The slits were set at 4 nm. The photolumines-

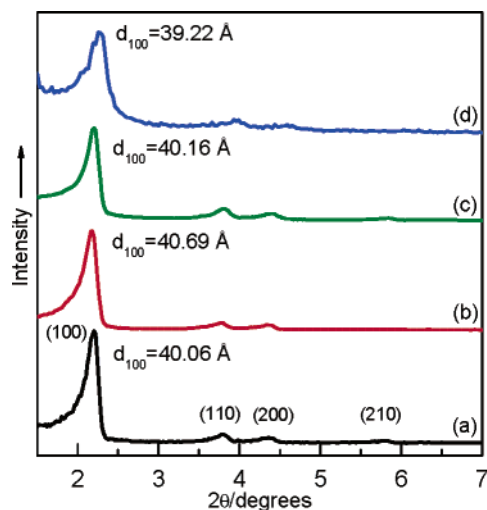


Figure 1. X-ray diffraction patterns in the low-angle region for the MCM-41 matrix at various steps: as synthesized, AS@MCM-41 (a); Zn^{2+} loaded, Zn@MCM-41 (b); ZnS loaded, ZnS@MCM-41 (c); and ZnS loaded heat treated, ZnSHT@MCM-41 (d).

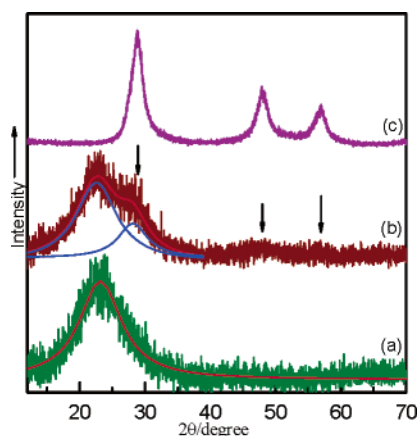


Figure 2. Wide-angle XRD patterns of as-synthesized AS@MCM-41 (a), ZnS@MCM-41 (b), and ZnS nanocrystallites with an average size of 3.8 nm (c).

cence excitation and emission spectra have been corrected through the instrument-supplied files, created from compounds with known quantum yields and an included Si photodetector. All optical UV-vis and PL spectra were recorded at room temperature.

3. Results and Discussion

Figure 1 shows the XRD patterns of MCM-41 material at various stages of preparation within the 2θ range $1.5\text{--}7^\circ$. As shown in this figure, all the XRD patterns of the sample in various preparation steps display four reflection peaks, typical of MCM-41 materials. Specifically the patterns (a), (b), and (c) show a characteristic strong reflection at low scattering angles 2θ , corresponding to a d_{100} spacing at about 40 Å. The calcined sample (d) presents a decrease (~ 1 Å) in the d_{100} spacing in relation to the unheated samples. The decrease in d_{100} reflects a small shrinkage in the pore diameters upon calcination. The aforementioned patterns indicate that the MCM-41 structure is maintained in all cases, even after heating (Figure 1d), providing good quality and a high range of uniform pores.

Figure 2 shows the XRD pattern in the wide-angle region, where the as-synthesized AS@MCM-41 (Figure 2a) exhibits only a broad reflection at about $2\theta = 23^\circ$, which is attributed to amorphous wall structure of MCM-41. On the other hand,

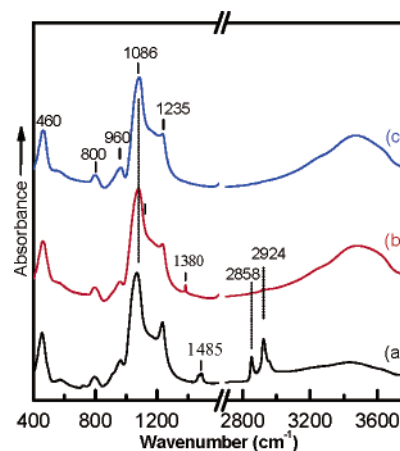


Figure 3. FT-infrared spectra of AS@MCM-41 (a), ZnS@MCM-41 (b), and ZnSHT@MCM-41 (c).

the pattern of ZnS@MCM-41 sample (Figure 2b) exhibits additional reflections at about 29° , 48° , and 57° which can be attributed to the (111), (220), and (311) lattice planes of zinc blende phases of ZnS [JCPDS No. 5-566]. From the full width at half-maximum of the (111) diffraction peak, obtained after curve fitting of the ZnS@MCM-41 XRD pattern within the 2θ range of $10\text{--}30^\circ$, the average size of the crystallites was estimated to be 1.6–1.8 nm, using Scherrer's equation. The as-calculated size of the nanoparticle seems to be in good agreement with that estimated from the UV-vis spectrum, as will be discussed further below.

The pattern of bulklike ZnS nanoparticles, Figure 2c, obtained by the direct chemical synthesis is also included in this figure for comparison. This exhibits, in relation to Figure 2b, relatively narrow reflection XRD peaks, which enable the accurate determination of the mean size. For instance, using Scherrer's equation for the first peak at 29° , it is found to correspond to a particle size of 3.8 nm.

Energy-dispersive analysis (EDS) indicated that the maximum achieved loading content of the ZnS nanoparticles inside the MCM-41 host was 9.3 ± 1.5 wt % (average of five different sample spots). The stoichiometric ratio for Zn and S was close to 1:1, whereas a small deviation of about 5% was observed which is due to the surplus amount of unreacted Zn^{2+} ions (ZnS@MCM-41). From this, it can be concluded that the samples have an excess of Zn, also discussed in the luminescence experiments. For the ZnS@MCM-41 sample the deviation was much larger at about 20%, which leads to sulfur-deficient quantum dots or smaller well-structured quantum dots.

The infrared spectra of the as-synthesized AS@MCM-41, after surfactant extraction and Zn^{2+} loading Zn@MCM-41, and the final solid with nanoparticles ZnS@MCM-41 are shown in Figure 3. Spectrum a from the synthesized sample shows bands at 1086, 960, 800, and 460 cm^{-1} . Bands at similar frequencies in the spectra of crystalline and amorphous SiO_2 have been assigned to characteristic vibrations of Si–O–Si bridges cross-linking the silicate network.^{24,25} Thus, the stronger band at 1086 cm^{-1} in Figure 3 can be assigned to the asymmetric stretching mode vibration of the Si–O–Si group, whereas the bending motion of oxygens in the same bridge is responsible for the band at 800 cm^{-1} (motion along the bisector of the Si–O–Si bridging group). In addition, the rocking motion of bridging oxygens perpendicular to the Si–O–Si plane can be correlated with the 460 cm^{-1} band. Evidence for the surfactant extraction after the exchange reactions with the ammonium and zinc salt comes also from Figure 3. Thus, the parent AS@MCM-41 solid

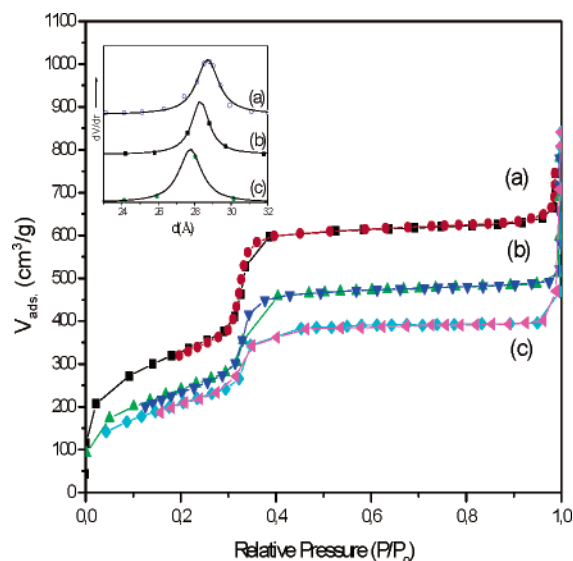


Figure 4. Nitrogen adsorption-desorption isotherms for HTMCM-41 (a), ZnMCM-41 (b), and ZnS/MCM-41 (c). Inset: pore distributions calculated from N₂ adsorption branches.

exhibits strong absorption bands below 3000 cm⁻¹ assigned to the -CH₃ and -CH₂- aliphatic moieties of the surfactant cations that are totally vanished after the exchange reactions with Zn(NO₃)₂·6H₂O. In addition, a new weak band at 1380 cm⁻¹ appears and it is attributed to the presence of some amount of compensated NO₃⁻ ions in the solid. These data clearly point to template removal and simultaneous grafting of mobile, ion exchange derived, Zn²⁺ species onto the MCM-41 surfaces through its -Si-O⁻ and -Si-OH groups. Additionally, they signify the uniform distribution of the inserted species mainly over the internal walls of the silica support where the majority of the surfactant molecules were protruded. The removal of surfactant template is evident mainly from the high-frequency part of the spectrum where the absorption bands at 2924 and 2858 cm⁻¹, from the asymmetric and symmetric vibrations of CH₂ units, as well as the high-frequency shoulder in the 2924 cm⁻¹ band, from the asymmetric vibration of CH₃ group, vanish after the exchange reactions. In addition, the bands centered at about 1480 cm⁻¹, which are due to the bending vibrations of CH₂ and CH₃ units, also disappear. Upon H₂S treatment of the ZnMCM-41 solid, no significant changes were observed in the IR spectra (Figure 3c) except the vanishing of the 1480 cm⁻¹ band because the nitrates can be exchanged with the sulfur anions.

The N₂ adsorption-desorption isotherms for a calcined MCM-41 sample (HTMCM-41) (a), the Zn²⁺-loaded (ZnMCM-41) (b), and the ZnS-loaded (ZnS/MCM-41) (c) and the corresponding pore size distribution curves are shown in Figure 4. The isotherms are all type IV classification, which is characteristic of mesoporous material adsorption. The presence of a sharp sorption step in adsorption curves, near a 0.3 value of P/P_0 , indicates that all solids possess a well-defined array of regular mesopores. The surface areas of the samples were calculated using the BET equation or, alternatively, by the “*t*-plot” method developed by de Boer et al.,²⁶ which also allows the determination of the external surfaces of the solids. The

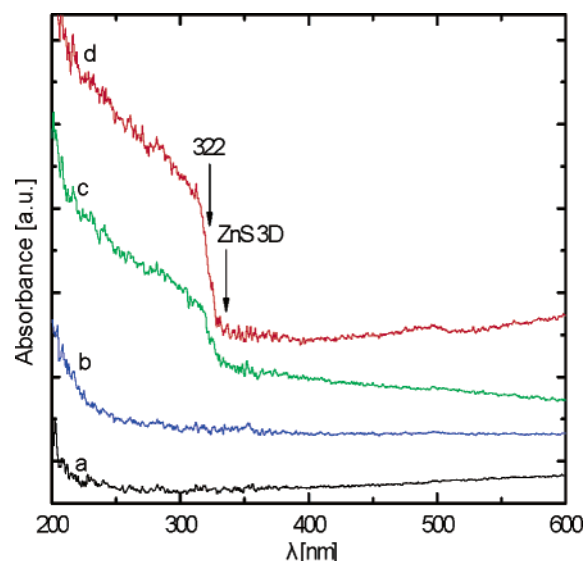


Figure 5. Absorbance spectra of unloaded AS/MCM-41 (a), ZnMCM-41 (b), and ZnS/MCM-41 (c, d). Spectrum c corresponds to a sample with larger quantum dots.

adsorption branch was used to calculate mesopore size distributions by means of the Barrett-Joyner-Halenda (BJH) method.²⁷ The basic parameters of the pore structure for the three samples, calculated from these data, are listed in Table 1.

As shown in this table, the heat-treated HTMCM-41 sample exhibits a high surface area (S_{BET} and S_t) of 1156 m²/g, while from the PDS curve its mean pore diameter was calculated to about 29 Å. In comparison to that, the ZnMCM-41 (uncalcined and after surfactant ion exchange with Zn ions; Figure 4b) has a decrease of its surface area that is now 755 m²/g while the pores of this sample show a size distribution with a average pore diameter of 28.3 Å. Moreover, the surface area of the ZnMCM-41 sample decreases further (642 m²/g) after exposure of the sample in H₂S gas (Figure 4c), which provides evidence that the pores are filled with ZnS nanoparticles. The fact that the isotherm for the ZnS/MCM-41 sample is similar in shape to that of the parent sample suggests that the ZnS nanoparticles should be dispersed uniformly throughout the pores.

Figure 5 shows the UV-vis absorbance spectra obtained as described in the Experimental Section. Optical measurements reveal information about the nature of the semiconductor nanoparticles, such as the energy gap (E_g), the type of the quantum confinement of the electron and hole, defect/trap centers, size, and the incorporation environment. In the latter case, the effects observed are dependent on energy transfer phenomena or alteration of the optical properties due to the dielectric constant of the surrounding medium. In this way it is possible to tune the dots and the host environment for specific properties or applications. Thus, it is necessary to first optically characterize the semiconductor properties of the quantum dots within the inert matrix and second compare the current optical properties to those of further research works altering the dot itself or the environment. Figure 5a shows the absorption of the AS/MCM-41 sample, where no absorbance is observed from 200 to 600 nm. Figure 5b shows the absorbance of the

TABLE 1: Pore Parameters Derived from N₂ Adsorption Data

samples	S_{BET} (m ² /g)	S_t (m ² /g)	S_{ext} (m ² /g)	S_{pore} (m ² /g)	V_{pore} (cm ³ /g)	d_{BJH} (nm)
HTMCM-41	1156	1110	71	1039	0.985	2.87
ZnMCM-41	755	705	62	643	0.753	2.83
ZnS/MCM-41	642	630	45	585	0.612	2.78

ZnS/MCM-41 samples, where again no peaks are detected in the same spectral region. Spectra c and d, respectively, of Figure 5 show the absorbance of ZnS/MCM-41 and ZnS_d/MCM-41 samples, which exhibit an absorbance onset at about 322 nm (dotted arrow in this figure), with no other peaks in the region from 340 to 800 nm. The two spectra (Figure 5c,d) differ in the profile and the onset position, which suggests that the two composites must differ with respect to the semiconductor particle size. This is in agreement with the EDS analysis of the two corresponding samples because the ZnS_d/MCM-41 (Figure 5d) has an excess of Zn and less sulfur than the ZnS/MCM-41 sample (Figure 5c); thus, it is expected that the formed quantum dots will be smaller. In this figure, a vertical arrow points to the position of the bulk ZnS energy gap absorbance, i.e., 3.7 eV, which is taken from ref 28 and takes into account the discussion in ref 29 while some authors report it at lower energies.¹⁶ The ZnS-loaded samples do not seem to possess any distinct peaks, possibly excitonic peaks, in the region of 200–300 nm, but rather a steplike absorbance onset from 300 nm down to 200 nm. This seems to be characteristic of a sample where the maximum size (R_{\max}) of the formed quantum dots exhibits a blue shift at the observed onset, but there are also nanoparticles, being formed inside the pores, of smaller than R_{\max} radii. For the calculated mean value of the particle size derived from Scherrer's equation, it must be noted that the methodology implies the existence of a nanoparticle percentage larger than this, which is in agreement with the presented UV–vis spectra. The calculated size of about 1.8 Å is responsible for band gap absorption onsets, for ZnS, at much lower wavelengths than 322 nm. Further, an estimate and discussion for R_{\max} are being presented.

The observed blue shift of ca. 25 nm, i.e., the shift of the energy gap of the QD with respect to the bulk value, is explained by the size quantization effect, where the energy gap, and sometimes the excitonic binding energy (E_b), of a LD semiconductor increase as the dimensionality is decreased. The bulk ZnS exciton cannot be distinguished as a separate peak at room temperature; $E_b \approx 40$ meV.²⁹ In the ZnS QD E_b is much higher, $E_b \approx 0.4$ – 0.9 eV,³⁰ and it is expected that it will further increase, through the dielectric confinement effect, since the matrix has lower ϵ than ZnS³¹ or decrease if the environment of the host prevents the total confinement of the electron and/or the hole.³² These blue shift and absorbance spectra results are in agreement with similar results for ZnS-loaded MCM-41 samples or ZnS nanoparticles.^{16,21,22}

Details of the spectra of Figure 5c,d show that the ZnS_d/MCM-41 sample, with the smaller QD radii, exhibits a well-defined absorption step at 315 nm, where the sample in Figure 5c exhibits the same type step at 320 nm. These small shifts, along with later discussed luminescence spectra and the chemical analysis of the composite, provide more evidence as proof of the formation of ZnS QD and the accompanying quantum confinement effect.

Therefore, from the optical spectra analysis, we can conclude that the MCM-41 is loaded with ZnS nanoparticles that have formed inside the cylindrical pores of the matrix. If the nanoparticles had formed outside the MCM-41 cylinders, then it is obvious that their radii would have a size distribution from atomlike to such a value providing the dots with bulklike optical properties. In this hypothetical case, the optical properties would have been the convolution of the size distribution with the respective optical properties and therefore the onset peak of the Figure 5c or Figure 5d spectrum would have been less steep and less sharp, due to the fact that larger nanoparticles have

energy gap onsets larger than the observed 322 nm onset and would have appeared at larger wavelengths.

Also, had the formation of particles taken place outside the pores, then it would not have been possible to observe the varying quantum confinement effect, as for samples in Figure 5c,d, especially when the loading of the MCM-41 is about 10%. If ZnS had formed in an appreciable quantity outside the pillars or in a nonuniformly spread pattern, then the high loading would have forced the formation of particles with bulklike properties and the luminescence spectra would have been different, as discussed further on.

It is well-known that, under certain assumptions, analytical equations can relate the energy gap and the excitonic binding energy to the geometric size, static dielectric constant, and electron/hole properties of an LD system. In the case of ZnS, formula eq 1 can be used,^{33,34} based on the original derived in various ways by authors in refs 35 and 36, to determine the radius R of a spherical quantum dot given the blue shift of the energy gap (ΔE).

$$\Delta E = \frac{\hbar^2 \pi^2}{2\mu R^2} - 1.786 \frac{e^2}{\epsilon_{\text{QD}} R} \quad (1)$$

For the reduced mass of the electron/hole pair there is a multitude^{29,37–42} of experimental and theoretical values, based on the values of bulk ZnS, which has a light electron in the conduction band and a light as well as a heavy hole in the valence band. The onset of the absorption is attributed, first, to the heavy hole effects, and we have implemented the values $m_e = 0.34m_0$, $m_{\text{lh}} = 0.25m_0$, and $m_{\text{hh}} = 0.94m_0$, while for the static dielectric constant of nanoparticle we have implemented a size-dependent expression according to the formula of ref 43 in eq 2, as it is normal to expect that the QD is not really the same structure as the bulk ZnS.

$$\epsilon_{\text{QD}} = 1 + \frac{\epsilon_{3\text{D}} - 1}{1 + \frac{\Delta E^2}{E_g^2}} \quad (2)$$

where $\epsilon(3\text{D})$ is taken to be the bulk dielectric constant of 8.3 and ΔE is computed with the bulk absorption starting at 340 nm. Other dielectric function methodologies have been proposed;⁴⁴ however, these include parameters that cannot be included in the indirect way eq 2 proposes. In this skeptic, R is computed to have an upper bound $R \sim 2.0$ nm, which is higher than the value computed for the size of the nanoparticles from the XRD patterns.

Assuming that the quantum dot model is valid, i.e., confinement in 3D, the discrepancy could be from the fact that the quantum dots are not spherical, but rather are cylindrically shaped particles due to the growth limitation imposed by the MCM-41 template. In this case, the mean value of the particle size, from implementation of Scherrer's equation, is quite probably related to a mean value of the two dimensions characterizing a nonspherical particle.⁴⁵ Accurate knowledge does not exist for the dielectric constant and effective hole and electron mass for the quantum dot system; neither is there a solid theoretical model for anisotropic quantum dots. However, various choices for the effective masses or the dielectric constant do not suffice to vary the value of the calculated R_{\max} to that of the XRD-derived value. In this aspect, it is more reasonable to assume that the quantum dot nanoparticles can be resembled, although cylindrical-like, as quantum dots with such optical properties as those of quantum dot spheres with $R \sim 2$ nm.

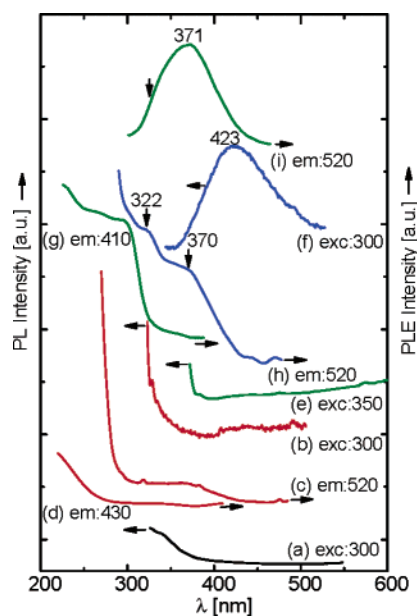


Figure 6. PL (left) and PLE (right) spectra for AS \otimes MCM-41 (a, excitation 300), Zn \otimes MCM-41 (b, excitation 300; c, emission 520; d, emission 430), ZnS \otimes MCM-41 (e, excitation 350; g, emission 410; i, emission 520), and ZnS $_d$ \otimes MCM-41 (f, excitation 300; h, emission 520).

It can be also argued that the quantum dots, grown as cylinder-like, are neither zero dimensional (quantum dot, 0D) nor one-dimensional (quantum wire, 1D). It is well-known that a semiconductor of dimensionality between 0D and 1D has absorbance peaks higher than the analogous 0D system and lower than the 1D system.² Thus it is logical to assume that the observed absorbance onset at 322 nm may well be attributed to anisotropic, cylinder-like, quantum dots and thus appears at larger wavelengths than the absorption edge of a spherical quantum dot (0D). It must be noted that from the XRD data it is not possible to distinguish between the spherical or cylindrical shape of the quantum dots since the use of Scherrer's equation is applicable in both cases, as has been discussed in ref 45. Therefore, in this hypothetical argument, the same result is derived that the quantum dots are merely anisotropic rather than spheres.

Figure 6 shows the photoluminescence (PL) and photoluminescence excitation spectra (PLE) for the AS \otimes MCM-41 host, Zn \otimes MCM-41, and ZnS \otimes MCM-41 samples. Photoluminescence (PL) spectra of quantum dots are a more complex phenomenon than those of higher dimensionality LD semiconductor structures, without considering ZnS PL spectra complications.⁴⁶ In this paper, photoluminescence at room temperature provides extra evidence about the energy gap, and the energy levels within the semiconductor energy gap. Especially PLE spectra can confirm the nature of the emission peaks which all extend to portraying information about the atomic structure, the formation or not of defect-free quantum dots as well as providing basic characterization of the emission properties for applications of the QD. PL/PLE spectra also include details from possible Zn²⁺ ions⁴⁷ and clarify effects that are due to the MCM luminescence.⁴⁸ Figure 6a displays the luminescence of the AS \otimes MCM-41 under excitation of 300 nm, corresponding to energy higher than the band gap of ZnS QD. It is observed that only a tail of the Rayleigh scattering is seen up to 320 nm, while no other peaks are detected in the spectral region between 320 and 600 nm. This result, compared to the luminescence of heat-treated MCM-41,⁴⁸ is found to be different since in this work the siliceous host is not thermally treated and, therefore,

does not contain luminescence centers but does contain organic material responsible for luminescence quenching of the surface states within the pores. The matrix does not show luminescence at lower excitation energies.

Figure 6b shows the PL spectrum of Zn \otimes MCM-41 under the excitation of $\lambda_{\text{exc}} = 300$ nm. We observe that there are again no noticeable peaks in the region 320–600 nm, except for a very small broad peak in the region of 400–450 nm, which has been observed also for lower energy excitations, i.e., $\lambda_{\text{exc}} \sim 350$ nm. To further analyze this peak, PLE measurements have been performed, shown in spectra c and d, respectively, of Figure 6 at the emissions of 520 and 430 nm. At the emission of $\lambda_{\text{em}} = 430$ nm there are no peaks in the PLE spectrum in the region of 300–400 nm, while for the 520 nm emission we observe a small shoulder at about 370 nm. This is perhaps owed to the appearing luminescence properties of the MCM-41 matrix, since the organic molecules (PL quenchers) have been removed, as discussed in ref 48. It must be noted that no peaks are detected close to the band gap of the larger QD, i.e., in the region of 300–320 nm. The structures of the spectra do not indicate that this is due to Zn luminescence.⁴⁹

Figure 6e and Figure 6f show the PL spectra of the ZnS \otimes MCM-41 and ZnS $_d$ \otimes MCM-41 samples for excitations at 350 and 300 nm, respectively. For excitation energy less than the QD energy gap ($\lambda_{\text{exc}} = 350$ nm) we observe that we have no luminescence, while for excitation energy above the QD energy gap ($\lambda_{\text{exc}} = 300$ nm) we observe an intense peak at 423 nm, which is in agreement with other research works on ZnS quantum dots and can be assigned to surface defects.^{16,21} More specifically, it is accepted that sulfur vacancies are the source of the 423 nm band, which is logical since our samples have been analyzed to possess an excess of Zn²⁺.

To further clarify the emission band and verify the quantum dot luminescence origin, we have performed PLE measurements at the emission wavelengths of 410 (Figure 6g) and 520 nm (Figure 6h,i). The first energy corresponds to emission from the highest energies of the defect band, within the energy gap of the semiconductor, while the second energy corresponds to emission from the lowest states. We observe that for the large quantum dot system, composite ZnS \otimes MCM-41 (Figure 6g,i), the emission at 410 nm is due to an absorption at 300 nm, related to the band gap of the quantum nanoparticles, while the emission at 520 nm is due to a strong absorption at 370 nm and a small shoulder that is seen at ca. 320 nm. Obviously the PLE spectra emission at 410 nm, provided in Figure 6g, shows that the only mechanism leading to luminescence at the top of the 423 nm band is the band gap absorption/and or excitons being formed, as observed from the onset of the PLE spectrum at 300 nm.

For the composite system with small quantum dots, ZnS $_d$ \otimes MCM-41, we observe that we have emission at 520 nm (Figure 6h) resulting from absorption at the 370 nm band as well as from a distinct absorption peak at 322 nm, which is obviously related to the exciton and absorption edge of the quantum dots.

The ZnS \otimes MCM-41 and ZnS $_d$ \otimes MCM-41 samples are therefore observed to have different luminescence properties from the precursor samples, mainly by observing the intensity of the 423 nm band and the PLE peak at 300–320 nm. The PLE peaks are in accordance with the corresponding absorption spectra and are related to the formation of semiconductor quantum dots.

The differences in the PLE spectra between the samples with small and large nanoparticles is that the overall smaller nanoparticle composite may have its larger radius quantum dots formed with fewer defects, and thus the defect mechanism

responsible for the luminescence at 420 nm may be better driven to excitation from the band gap/and or the formed excitons rather from intermediate band gap states.

4. Conclusions

In summary, a new route for synthesizing ZnS quantum dots inside the pores of MCM-41 has been reported. The synthesis method was based on effective melt exchange reactions. The ZnS quantum dots have been characterized with respect to their optical properties and are attached in the inner surfaces of the siliceous mesoporous matrix, which retains significant porosity and hexagonal porous structure after the ZnS incorporation. Effort has been made toward understanding the optical properties with the basic bulk semiconductor parameters. Therefore, the final composite has both porous and semiconducting properties, making it ideal for novel applications demanding high surface area and active optical surface states. The latter can be tuned by means of extra surface passivation or doping of the ZnS active semiconductor.

Acknowledgment. The work was supported in part from a collaboration program awarded from the General Secretariat for Research and Technology of Greece.

References and Notes

- (1) Green, M.; Brien, P. O. *Chem. Commun.* **1999**, 2235.
- (2) Papavassiliou, G. C. *J. Solid State Chem.* **1981**, *40*, 330.
- (3) Berry, C. R. *Phys. Rev.* **1967**, *161*, 848.
- (4) Ekimov, A. I.; Onuschchenko, A. A.; Tsekhomskii, V. A. *Fiz. Khim. Stekla* **1980**, *6*, 51.
- (5) Wang, Y.; Herron, N. *J. Phys. Chem.* **1987**, *91*, 257.
- (6) MacDougall, J. E.; Eckert, H.; Stucky, G. D.; Herron, N.; Wang, Y.; Moller, K.; Bein, T.; Cox, D. *J. Am. Chem. Soc.* **1989**, *111*, 8006.
- (7) Garcia, M. M.; Villavicencio, H.; Hernandez-Velez, M.; Sanchez, O.; Martinez-Duart, J. M. *Mater. Sci. Eng., C* **2001**, *15*, 101.
- (8) Wazke, H. J.; Fendler, J. H. *J. Phys. Chem.* **1987**, *91*, 854.
- (9) Hirai, T.; Okubo, H.; Komasa, I. *J. Colloid Interface Sci.* **2001**, *235*, 358.
- (10) Kortan, A. R.; Hull, R.; Opila, R. L.; Bawendi, M. G.; Stiegerward, M. L.; Carrol, R. J.; Brus, L. E. *J. Am. Chem. Soc.* **1990**, *112*, 1327.
- (11) Stiegerward, M. L.; Alevisatos, A. P.; Gibson, J. M.; Harris, T. D.; Kortan, R.; Muller, A. J.; Thayer, A. M.; Duncan, T. M.; Douglas, D. C.; Brus, L. E. *J. Am. Chem. Soc.* **1988**, *110*, 3046.
- (12) Wang, Y.; Suna, A.; Mahler, W.; Kasowski, R. *J. Chem. Phys.* **1987**, *87*, 7315.
- (13) Savchuk, A. I.; Fediv, V. I.; Kandyba, Ye. O.; Savchuk, T. A.; Stolyarchuk, I. D.; Nikitin, P. I. *Mater. Sci. Eng., C* **2002**, *19*, 59–62.
- (14) Abe, T.; Tachibana, Y.; Uematsu, T.; Iwamoto, M. *Chem. Commun.* **1995**, 1617.
- (15) Zhang, W.-H.; Shi, J.-L.; Wang, L.-Z.; Yan, D.-S. *Chem. Mater.* **2000**, *12*, 1408.
- (16) Zhang, W.-H.; Shi, J.-L.; Wang, L.-Z.; Chen, H.-R.; Hua, Z.-L.; Yan, D.-S. *Chem. Mater.* **2001**, *13*, 648.
- (17) Zang, Z.; Dai, S.; Fan, X.; Blom, D. A.; Pennycook, S. J.; Wei, Y. *J. Phys. Chem. B* **2001**, *10*, 6755.
- (18) Beck, J. S.; Vartuli, J. C.; Roth, W. J.; Leonowicz, M. E.; Kresge, C. T.; Schmitt, C. T.; Chu, C. T.-W.; Olson, D. H.; Sheppard, E. W.; McCullen, S. B.; Higgins, J. B.; Schlenker, J. L. *J. Am. Chem. Soc.* **1992**, *114*, 10834.
- (19) Kresge, C. T.; Leonowicz, M. E.; Roth, W. J.; Vartulli, J. C.; Beck, J. S. *Nature* **1992**, *359*, 710.
- (20) Agranovich, V. M.; LaRocca, G. C.; Bassani, F. *JETP Lett.* **1997**, *66*, 748.
- (21) Chae, W.-S.; Yoon, J.-H.; Yu, H.; Jang, D.-J.; Kim, Y.-R. *J. Phys. Chem. B* **2004**, *108*, 11509.
- (22) Rana, R. K.; Zhang, L.; Yu, J. C.; Mastai, Y.; Gedanken, A. *Langmuir* **2003**, *19*, 5904.
- (23) Bourlino, A. B.; Karakassides, M. A.; Gournis, D.; Georgakilas, V.; Moukarika, A. *Chem. Lett.* **2003**, *32*, 38.
- (24) Kirk, C. T. *Phys. Rev. B* **1988**, *38*, 1255.
- (25) Almeida, M. R.; Pantano, C. G. *J. Appl. Phys.* **1990**, *68*, 4225.
- (26) Lippens, B. C.; DeBoer, J. H. *J. Catal.* **1965**, *4*, 319.
- (27) Barrett, E. P.; Joyner, L. G.; Halenda, P. H. *J. Am. Chem. Soc.* **1951**, *73*, 373.
- (28) Nanda, J.; Sarma, D. D. *J. Appl. Phys.* **2001**, *90*, 2504.
- (29) Tran, T. K.; Park, W.; Tong, W.; Kyi, M. M.; Wagner, B. K.; Summers, C. J. *J. Appl. Phys.* **1997**, *81*, 6.
- (30) Einevoll, G. T. *Phys. Rev. B* **1992**, *45*, 3410.
- (31) Keldysh, L. V. *JETP Lett.* **1979**, *29*, 658.
- (32) Zhu, J. L.; Zhu, S.; Zhu, Z.; Kawazoe, Y.; Yao, T. *J. Phys.: Condens. Matter* **1998**, *10*, 583.
- (33) Yin, J. X.; Yan, J.; Zhi-lin, Z.; Xu, S.-H. *J. Cryst. Growth* **1998**, *191*, 692.
- (34) Denzler, D.; Olschewski, M.; Sattler, K. *J. Appl. Phys.* **1998**, *84*, 2841.
- (35) Brus, L. E. *J. Chem. Phys.* **1984**, *80*, 4403.
- (36) Kayanuma, Y. *Phys. Rev. B* **1988**, *38*, 9797.
- (37) Klein, W. *Phys. Rev. B* **1981**, *24*, 3493.
- (38) Shahzad, K.; Olego, D. J.; Van de Walle, C. G. *Phys. Rev. B* **1988**, *38*, 1417.
- (39) Logue, F. P.; Rees, P.; Heffernan, J. F.; Jordan, C.; Donegan, J. F.; Hegarty, J. *J. Opt. Soc. Am. B* **1998**, *15*, 1295.
- (40) Ichino, K.; Ueyama, K.; Kariya, H.; Suzuki, N.; Kitagawa, M.; Kobayashi, H. *Appl. Phys. Lett.* **1999**, *74*, 3486.
- (41) Wageha, S.; Shu-Mana, L.; Youa, F. T.; Xu-Rong, X. *J. Lumin.* **2003**, *102*, 768.
- (42) Senger, R. T.; Bajaj, K. K. *Phys. Status Solidi B* **2004**, *241*, 1896.
- (43) Tsu, R.; Babic, D.; Ioratti, L. *J. Appl. Phys.* **1997**, *82*, 1327.
- (44) Yoffe, A. D. *Adv. Phys.* **2001**, *50*, 1.
- (45) Kumpf, C.; Neder, R. B.; Niederdraenk, F.; Luczak, P.; Stahl, A.; Scheuermann, M.; Joshi, S.; Kulkarni, S. K.; Barglik-Chory, C.; Heske, C.; Umbach, E. *J. Chem. Phys.* **2005**, *123*, 224707.
- (46) Yin, L. W.; Bando, Y.; Zhan, J.-H.; Li, M. S.; Goldberg, D. *Adv. Mater.* **2005**, *17*, 1977.
- (47) Denzler, D.; Olschewski, M.; Sattler, K. *J. Appl. Phys.* **1998**, *84*, 2842.
- (48) Shen, J. L.; Cheng, C. F. *Curr. Opin. Solid State Mater. Sci.* **2003**, *7*, 427.
- (49) Chang, S. S.; Yoon, S. O.; Park, H. J.; Sakai, A. *Mater. Lett.* **2002**, *53*, 432.